Research Article

The Journal of Comparative Neurology
Research in Systems Neuroscience
DOI 10.1002/cne.24212

Anatomical segmentation of the human medial prefrontal cortex

Córcoles-Parada M[1], Müller NCJ[2], Ubero M [1], Serrano-del-Pueblo VM[1], Mansilla F[3], Marcos-Rabal P[1], Artacho-Pérula E[1], Dresler M[2], Insausti R[1], Fernández G[2], Muñoz-López M[1]

[1]Human Neuroanatomy Laboratory and Regional Centre for Biomedical Research, School of Medicine, University of Castilla-La Mancha, Albacete, Spain.

[2]Donders Institute for Brain, Cognition and Behaviour, Radboud University Medical Centre, Nijmegen, The Netherlands.

[3]Radiology Service, Sta. Cristina Clinic and University Hospital of Albacete, Albacete, Spain.

Corresponding author: Mónica Muñoz-López. Human Neuroanatomy Laboratory, School of Medicine and Regional Centre for Biomedical Research (CRIB), University of Castilla-La Mancha, Ave. Almansa, 14, 02006 Albacete, Spain. Phone: +34 902204100 ext. 2962. monica.munozlopez@uclm.es

Key words: Medial prefrontal cortex, anterior cingulate cortex, area 24, area 32, area 14, area 25, MRI, structural segmentation. RRIDs: SCR_002010, SCR_004757, SCR_001847, SCR_002078, SCR_014288.

Conflict of interest: The authors of this work have no conflict of interest to declare.

Acknowledgements: Supported by the Spanish Government Institute Carlos III (FIS PI11/02860), University of Castilla-La Mancha (UCLM) mobility grant VA13815001497 and Erasmus+ grants to M. Muñoz and M. Córcoles at the Donders Institute for Brain, Cognition and Behaviour, Radboud University Medical Centre, Nijmegen, The Netherlands. Thanks to Michael Czisch for providing the *in vivo* MRI scans and to Joaquín González-Fuentes and Sandra Cebada-Sánchez for providing some of the *ex vivo* cases. Thanks to Mercedes Iñiguez and Isidro Medina for their technical assistance, to the UCLM medical summer students Cristina Aguado and Santos Ibáñez for their collaboration in this study, and to Richard Morris for his comments on this manuscript. Special thanks are due to all the participants, the donors, and their families.

Received: Sep 14, 2016; Revised: Feb 26, 2017; Accepted: Mar 13, 2017

Author contributions

M Muñoz-López conceived and designed the study, secured the funding, and contributed to all the different phases of the study, from brain tissue processing and microscopy through to MRI data acquisition and its analysis, and preparing the manuscript and figures. M Córcoles-Parada processed the brain tissue, took photographs, built unfolded maps and completed the *ex vivo* and *in vivo* MRI analysis including segmentation of mPFC areas, measurement of volumes, cortical full length, and distances. M Córcoles-Parada prepared parts of the manuscript and figures as part of her PhD thesis. NCJ Müller, M Dresler, and G Fernández contributed to the MRI side of the study by providing the *in vivo* MRI scans, processing the MRI data to visualize sulci, generating probabilistic maps and contributing critical ideas during the preparation of the results. M Ubero participated in the segmentation of mPFC of some *in vivo* cases, as well as preparation of the manuscript and figures. VM Serrano-del-Pueblo used some of the data for his MSc thesis and contributed to setting up the MRI data pre-processing pipeline for the segmentation of mPFC segmentation of *in vivo* MRI scans. F Mansilla, the clinical neuroradiographer, obtained the *ex vivo* MRI scans. R Insausti, P Marcos-Rabal, and E Artacho-Pérula contributed with the human brain tissue, the MRI scans of the *ex vivo* cases, and preparation of the study.

Abbreviations

ACC	Anterior cingulate cortex
AC-PC	Anterior-Posterior commissure
apos	Anterior parolfactory sulcus
BA	Brodmann's area
BOLD	Blood-oxygen-level dependent
cc	Corpus callosum
CG	Cingulate gyrus
cs	Cingulate sulcus
CSL	Cortical surface length
DLPFC	Dorsolateral prefrontal cortex
fMRI	Functional magnetic resonance imaging
ics	Intracingulate sulcus
ICV	Intracranial volume
irs	Inferior rostral sulcus
mPFC	Medial prefrontal cortex
MRI	Magnetic resonance imaging
OBFC	Orbitofrontal cortex
os	Olfactory sulcus
pcs	Paracingulate sulcus
PCG	Paracingulate gyrus
PFC	Prefrontal cortex
ROI	Region of interest
srs	Superior rostral sulcus

List of Research Resource Identifiers

ITK-Snap imaging software for segmentation: RRID:SCR_002010

ANTS - Advanced Normalization ToolS, RRID:SCR_004757

FreeSurfer, RRID:SCR_001847

Adobe Photoshop CS2, RRID:SCR_002078

Canvas, RRID:SCR_014288

Abstract

The medial prefrontal areas 32, 24, 14, and 25 (mPFC) form part of the limbic memory system, but little is known about their functional specialization in humans. To add anatomical precision to structural and functional MRI data, we aimed to identify these mPFC subareas in histological preparations of human brain tissue, determine sulci most consistently related with mPFC areal boundaries, and use these sulci to delineate mPFC areas in MRIs. To achieve this, we obtained 3D MRI data from 11 *ex vivo* hemispheres and processed them for cyto- and myelo-architectonic analysis. The architectonic boundaries of mPFC areas were identified in histology and cortical surface length and volumes were measured. Unfolded maps of histologically determined boundaries were generated to identify the association of mPFC areal boundaries with sulci across cases. This analysis showed that cingulate and superior rostral were the sulci most consistently related to mPFC areal boundaries. Based on presence/absence and anastomosis between such sulci, 6 sulci patterns in the 11 hemispheres were found. A further analysis of 102 hemispheres of *in vivo* MRI scans (N=51 males, mean±sd 24.1±3.1 years of age) showed similar sulci patterns, which allowed us to delineate the mFPC areas in them. The volumes of mPFC areas across histological, *ex vivo* and *in vivo* MRI delineations were comparable and probabilistic maps generated from the MRIs of the102 hemispheres. Probabilistic maps of mPFC areas were registered to MNI space and are available for regional analysis of fMRI data.

INTRODUCTION

Segmentation refers to the identification and delineation of an anatomical area or structure in magnetic resonance imaging (MRI). Anatomical guidelines for precise segmentation are critical for the establishment of the structural/functional integrity of a specific brain area in MRI scans in healthy and diseased brains. In memory research, the delineation of the different structures comprising the limbic system has received extensive attention. Within it, the hippocampus is the most extensively segmented structure in human MRI scans (Gadian et al., 2000; Yuskevich et al., 2015), with adjacent cortical regions such as the temporal pole, entorhinal, and perirhinal areas also successfully segmented (Insausti et al., 1998). However, the prefrontal components of the limbic memory system, such as the medial prefrontal cortex (mPFC), are still poorly defined in MRI scans and yet doing so is critical to better understand the anatomical underpinnings of neural disorders.

Atlases, standard templates, template spaces, and mathematical transformations are available for structural and functional brain imaging studies via SPM (Ashburner and Friston, 2000), FSL (FMRIB Software Library, Oxford, UK), or AFNI (Cox, 1996). These provide tools for automatic segmentation of different brain areas, including the mPFC. Although these methods allow critical comparisons across studies, they are limited in terms of precise anatomical localization at both the group and individual subject level. For example, the standard stereotaxic space developed by Talairach and Tournoux (Talairach and Tournoux, 1988) has been extensively used in many studies as a guideline for labelling (Lancaster et al., 1997; Lancaster et al., 2000). However, the cortical parcellations in human MRI based on it have been shown to be less than ideal predictors of some boundaries including those of higher order cortical areas (Amunts et al., 1999; Amunts et al., 2005). Limitations like these, together with interest in the determination of brain-function associations with classic maps based on architectonics (Rademacher et al., 2001; Roland et al., 2001; Van Essen, 2002), have stimulated the generation of new brain mapping techniques.

The two main types of methods for whole brain automatic segmentation are volume-based and surface-based. Volume-based cortical labelling tools include protocols developed at the Centre for Morphometric Analysis at the Massachusetts General Hospital (FreeSurfer, Fischl et al., 2002), the Montreal Neurological Institute MNI152

(Fonov et al., 2004, Petrides, 2012), the University of California´s Laboratory of Neuroimaging (LONI Brain Parser, Shattuck et al., 2008), as well as at the University Iowa Hospitals & Clinics (BRAINS, Brain Research: Analysis of Images, Networks, and Systems, Crespo-Facorro et al., 2000), and in London (Automated Anatomical Labeling - SPM, Statistical Parametric Mapping, Tzourio-Mazoyer et al., 2002). Some examples of surface-based human cortical labelling protocols are the "Mindboggle-101" dataset (Klein and Tourville, 2012), Desikan–Killiany (Desikan et al., 2006), and Destrieux protocols (Destrieux et al., 2010) used by the FreeSurfer brain analysis software (Dale et al., 1999; Fischl et al., 1999; Fischl et al., 2001; Fischl et al., 2002). These techniques are very helpful, but result in different areal segmentations, thereby making it a challenge to choose a particular method. A particular challenge arises when the aim is to measure volumes of specific areas in clinical cohort studies, in which individual values may indicate degree of damage. Identifying boundaries accurately requires a certain degree of confidence. Anatomically guided probabilistic maps have been introduced for the prefrontal cortex, but such maps are mostly available for regions within the lateral frontal cortex (Rajkowska and Goldman-Rakic, 1995; Amunts et al., 1999; Goulas et al., 2012). In the case of the mPFC, probabilistic maps have been provided for regional specific fMRI analysis (Mackey and Petrides, 2014; Palomero-Gallagher et al., 2015) but, to our knowledge, so far these only include the subgenual portion of the mPFC.

The aim of this study was to provide a method for segmentation of the mPFC in MRI scans that uses sulci, volumes, and cortical surface data from human brain histological material. To obtain this, a histologically-based set of quantitative and visual guidelines based on sulci and gyri were used to segment the pregenual, subgenual, and dorsal aspects of the mPFC areas 32, 24, 14, and 25 in MRI scans. This method of segmentation is laborious given that requires the manual segmentation of the individual mPFC areas in a subject-by subject bases. Nevertheless, it is the recommended one for studying changes in mPFC areas in diseased conditions at the individual level. To allow regional analysis of structural/fMRI studies at the group level, we segmented the mFPC in 51 MRI scans by means of the manual method described above. This procedure allowed us to generate probabilistic maps of mPFC areas that are now available in MNI space.

MATERIALS AND METHODS

Ethics

This study was conducted according with the World Medical Association ethical principles for research with humans (Helsinki, Finland, 1964), with the local Committee for Clinical Research at the University of Castilla-La Mancha (UCLM), School of Medicine, and the University Hospital of Albacete (Act 02/12). Ethical approval was granted by the Medical Faculty of the University of Munich (Germany) for the *in vivo* MRI study and The Donders Institute for Brain, Cognition and Behaviour, Radboud University Medical Centre, Nijmegen (The Netherlands).

Ex vivo tissue processing and MRI acquisition

The body donor program at UCLM (Human Anatomy) provided 11 brain hemispheres from neurologically intact individuals from both genders (7 males and 2 females) with a wide age range (mean age 52.8; sd 31.7). There was no evidence of vascular damage or other neuropathological findings that could mislead identification of the cytoarchitectonic boundaries. Despite the age range and gender, gyri and the architectonic features of mPFC subareas were constant. Also, the association of architectonic boundaries with sulci was constant across the ages included in this study. The measurements (volumes, distances, and cortical length), once normalized for brain size, were equivalent. These allowed us to segment the mPFC independently of age and gender. Both hemispheres were available in 4 cases, only the right hemisphere in 3 cases, and only the left hemisphere in 2 cases. Brains were fixed according to previous protocols (Insausti et al., 1995). Briefly, brains were extracted and fixed by immersion in 10% buffered formalin. One of the cases was fixed by perfusion with bilateral intracarotid perfusion that consisted in 21% of saline at room temperature, followed by cold 4% buffered paraformaldehyde at 4^0 C. Brains were then scanned with a 1.5T Optima MR 450W from General Electric; T1, 3D volumetry SPGR. The initial parameters (TR: 8.5 ms; TE: 3.2 ms; TI: 400 ms; slice thickness: 1 mm; gap: 0; isotropic matrix: 256x256x256; nex: 1; resolution 1x1x1, acquisition time= 7.28 min) were modified to optimize image quality in each case. One case was scanned at 3T with a similar sequence leading to a 1x1x1 mm resolution. Frontal lobes were then dissected

from the rest of the hemispheres by a perpendicular cut to the anterior and posterior commissures (AC-PC) axis at the caudal end of the subgenual region (area 25). In this study, prefrontal cortex (PFC) was, therefore, defined as the region extending from the frontal pole as far caudal as a perpendicular line to the AC-PC axis placed at the caudal boundary of the subgenual region (area 25). The brains were photographed, coronal blocks of 1 cm thickness were dissected, equilibrated with 30% sucrose in buffer, and frozen-cut at 50 μm thickness in a microtome coupled to a freezing unit. From the frontal pole, a one-in-10 series of coronal sections (one-in-500μm) were mounted for Nissl staining with thionin (Merck, Darmstad, Germany) and used for cytoarchitectonic analysis. Another one-in-10 consecutive series of sections were stained using the Gallyas protocol (Gallyas, 1971) and used for myeloarchitectonic analysis. Storage of human brain tissue was carried out as described previously (Insausti et al., 1995).

Cytoarchitectonic analysis and relationship with myeloarchitectonics

Cytoarchitectonic boundaries were identified microscopically in Nissl/Gallyas stained sections with an Olympus BX51 microscope equipped with a digital video camera (QImaging FAST 1396, Surrey, BC, Canada) and an image analysis system (Bioquant Nova, R&M Biometrics Inc., Nashville, TN, USA), and photographed (Nikon DS-Fi1) at a magnification of 1x. Our analysis was guided primarily by the nonhuman primate description of the mPFC (Barbas, 1992) and by the comparative studies of human and rhesus monkey by Petrides and Pandya (Petrides and Pandya, 1999; Petrides and Pandya, 2002). The nomenclature used for these boundaries agree with those of the recent work of Morecraft (Morecraft et al., 2012) on the anterior cingulate cortex and the premotor adjacent areas in rhesus monkey. Although the architectonic boundaries in the present work were identified in coronal sections, they were in accord with the description previously reported by Von Economo and Koskinas (2008) and by Mai (2015) in sections cut perpendicular to its principal axis.

Two-dimensional maps

Two-dimensional unfolded maps of the mPFC were constructed following the procedure described by Van Essen and Maunsell (Van Essen and Maunsell, 1980), with a slight modification; i.e. we used the pial/cortical surface instead of layer IV to unfold the cortex. Maps were built from Nissl-stained coronal sections through the mPFC at

intervals of 2 mm. Architectonic boundaries and sulci were marked. The unfolded maps made it possible to determine sulci that were consistently related with mPFC subareas boundaries across cases. Sulci associated with areal boundaries were then used as anatomical guidelines to manually place areal boundaries on MRI coronal slices (1 mm thickness).

Sulci of the mPFC

Sulci of the mFPC include the paracingulate (pcs), cingulate (cs), intracingulate (ics), superior rostral (srs), inferior rostral (irs), and anterior parolfactory sulci (*apos*, Figure 1). The 6 variations found in this study are described in figure 5 and its legend. The *pcs* is inconstant, but, when present, it bends externally around the cingulate gyrus (CG) and often divides into several segments that may take an oblique orientation to the AC-PC axis (see figure 5, *pcs* in deparate segments in 1, 2 and continuous in 3, 4, and 5). This sulcus often runs towards the subgenual region, where it may join the srs, as it happens in the case illustrated in figure 1. Variants of this pattern whereby *pcs* remains independent of s*rs* in the subgenual regions can be appreciated in figure 5 (see 5). The *cs* is constant in terms of its presence, and bends rostrally to the genu of the corpus callosum (cc) establishing the CG. Caudally, the *cs* runs dorsal and in parallel to the body of the cc while ventrally, in the subgenual region, it may be independent of srs or it may join it, extending caudally as a single sulcus (see 1 and 2 respectively in Fig. 5). The subgenual *cs* may end at the *apos*, located in the most caudal portion of the subgenual region, perpendicular to the rest of the mPFC sulci at very variable degrees of obliqueness. The *ics* is inconstant and appears within the CG (Fig 1, also in pattern 4 in Fig. 5). The *srs* runs ventral to the *cs* in the subgenual region and may join *pcs*, as figure 1 illustrates, or the *cs*. The *irs* runs ventrally to the *srs* and may appear as a single longitudinal sulcus or divided into several segments from rostral to caudal.

Manual segmentation of *ex vivo* brains, volume and cortical surface measurements

MRI scans were equated for luminance inhomogeneity using an N4 bias correction with a 3D slicer (Harvard University, Boston, MA, USA). This allows unbiased prefrontal grey and white matter classification by means of the active contour segmentation tool in ITK-SNAP (Yushkevich et al., 2006), initialized by a decision forest classifier trained

on examples of white and grey matter drawn by the user in a single slice. Tissue classifications were supervised and corrected. Volumes of whole PFC, and of each of the four mPFC subareas were measured in coronal sections every 1 mm from the *ex vivo* and *in vivo* MRI scans with ITK-SNAP. In addition, intracranial volume (ICV) was also measured in the *in vivo* MRI scans. The full cortical surface length (CSL, in mm) of each mPFC subarea and of the CG were measured in coronal sections with ImageJ (Schneider et al., 2012). To control for brain size, data were normalized as previously described (Insausti et al., 1998). Briefly, the correction factor used to normalize each individual measurement was calculated by dividing the overall mean PFC volume by the individual's PFC volume. We multiplied raw volumes and CSL by this correction factor. In addition, we calculated the volumes of each mPFC subarea and of the total PFC and expressed the former as percent of the second.

In vivo brain MRI acquisition, image analysis, and manual segmentation

In vivo MRI scans were obtained from 51 healthy subjects (males, mean±sd age=24.1±3.1years) using a 3T GE Discovery MR750 scanner with a 12-channel head coil. A standard localizer, coil calibration, and a 3D T1-weighted anatomical scan: TR 7.1 ms, TE 2.2 ms, slice thickness 1.3 mm, in-plane FOV 240 mm, 320×320x128 matrix, 12° flip angle. Sulci were reconstructed with FreeSurfer (Martinos Centre for Neuroimaging, Harvard Univ., Boston, MA, USA) and all hemispheres were classified, like in the *ex vivo* analysis, according to the patterns of *pcs*, *cs* and *srs*.

The 51 MRI scans were aligned in the AC-PC axis and the skull removed using the brain extraction tool from FreeSurfer. Luminance inhomogeneity was corrected with N4 bias correction (3D slicer, op cit.). The mPFC subareas were delineated manually using sulci and gyri as visual guides to anatomically identify the location of mPFC areas, as determined in the *ex vivo* cases. Two corrected measures guided the placement of the mPFC subareas in the *in vivo* MRI scans: a) distances from the frontal pole to the rostral and caudal limits of each mPFC subarea expressed as a percent of total length of mPFC, b) CSL of the each mPFC area in the *ex vivo* material.

ICV was extracted for all the subjects using SPM12 (Welcome Department of Imaging Neuroscience, London, UK). The volumes of the mPFC subareas were extracted from

both *ex vivo* and *in vivo* MRI scans with ITK-SNAP separately for each hemisphere and corrected for brain size as described above, but this time the normalization factor was obtained by dividing mean ICV by individual ICV. A statistical analysis of these volumes was carried out using SPSS (v.19). The shrinkage of the histological material was estimated by comparing *in vivo* and *ex vivo* total PFC volumes and MRI data was corrected. *Ex vivo* PFC mean volume was 23% smaller compared with the *in vivo* due to tissue shrinkage (t_{108}=-5.25; p<0.001, Table 1). Mean volume reduction of mPFC subareas ranged from 13.8 to 29.9% with an overall mean reduction of 21.8%. Given the similarity between the mean mPFC and PFC volume reduction, we used the latter to adjust the *ex vivo* volumes and CSL to the *in vivo* measurements.

Probabilistic maps

A study-specific brain template was generated with the 51 *in vivo* MRI scans with ANTs (PICSL, Philadelphia, PENN, USA) (Avants et al., 2008; Avants et al., 2010). The *in vivo* segmentations for each area according to the quantitative and visual guidelines obtained in the *ex vivo* cases (described earlier in this section), were also registered to this template and averaged to generate probabilistic maps. These maps encode the probability of a voxel being part of one specific area, ranging from 0 to 100%. Additionally, we generated a maximum probability map. In this map, each voxel of the mPFC gets the value of the area with the highest probability. All brains and segmentations were registered to the MNI space with ANTs. All registrations were carried out using the diffeomorphic symmetric image normalisation approach implemented in ANTs (Avants et al., 2008).

RESULTS

Cytoarchitecture of mPFC areas

The different patterns of presence, absence, and thickness of granular cell layer IV, as well as pyramidal cell density and size within layers IIIc and Va in Nissl stained sections, were used to recognize the boundaries between the subareas comprising the mPFC. Despite the generally poor myelination of the mPFC revealed by Gallyas stain, the relative predominance of radially oriented fibre bundles as well as the presence/absence of horizontal fibre plexuses (i.e. bands of Baillarger in deep layer III

or IV and in deep layer V) were different between subareas. These myeloarchitectonic features were complementary to the cytoarchitectonic differences and, therefore, allowed the delineation of the subareas in coronal sections based on both characteristics (Fig. 2).

Area 32. Area 32 lays just caudal to the frontal pole area 10 and ventral to areas 8/9 (Fig. 1 and 2). It occupies dorsally the paracingulate gyrus and ventrally the subgenual region of the mPFC. Area 32 borders ventrally with area 24. In terms of cytoarchitectonic features (Fig. 3, A/B and E/F), layer II in area 32 is broader, with higher cellular density, and clearer II/III border relative to area 24. The darkly stained pyramidal neurons of layer IIIc form a discontinuous and somewhat irregular band. In fact, layers IIIc and IV intermingle, and therefore, the III-IV boundary appears irregular. This characteristic layer IIIc in area 32 progressively looses its large pyramidal cells dorsally. Area 32 is considered as dysgranular and, although layer IV can be identified along the whole area, this layer is somewhat wider and better identifiable in the pregenual and subgenual portions where the granular cells form occasional horizontal striations than in its dorsal portion. Dorsally, the prominence of deep over superficial layers gets more balanced, acquiring a closer resemblance to the dorsal medial area 8. Dorsal to the cc, and especially at its most caudal levels, these latter features become progressively more patent. Layers V and VI are wide and contain small neurons darkly stained; a poorly formed layer Vc makes almost indistinct the limit between layers V and VI. Layer Vc is more identifiable in the dorsal aspect of area 32. Two key features of area 32 serve to identity the border with area 24, namely the presence in area 32 of large and darkly stained pyramidal cells in layer IIIc, and the presence of layer IV. Layer IV also serves to distinguish area 32 from the granular dorsal medial areas 10 and 8/9 and dorsal to the agranular area 24. In myelin stained sections, the darker appearance of the pregenual and dorsal postgenual portions of area 32 differentiate the boundary with area 24.

Area 24. Area 24 lays in the CG. Layer II is distinguishable, although layers II/III boundary is less evident than in area 32 (Fig. 3, C/D and G/H). Relative to area 32, layer III has lower cell density and lightly stained neurons, and lacks the characteristic deeply stained neurons seen in Layer IIIc of area 32. We found that the key cytoarchitectonic features of area 24 are the absence of layer IV (agranular) and the striking prominence

of layer Va. Without a layer IV, the limit between layers III and V is identifiable for the presence of large and darkly stained pyramidal neurons in layer Va. Layers V and VI are wide, with a distinguishable boundary between them.

Area 14. This area occupies most of the gyrus rectus and is the one with the least limbic architectonic appearance (Fig. 3, I/J). The lower cell density in layer III is a key feature and makes a clear boundary with areas 10 and 32. Layer IV is present but appears narrower and less identifiable than in area 10. Two key features distinguish area 14 from 32: first, layer II has a poorly defined border with layer III that contrasts with the clear boundary in layers II-III in area 32; secondly, the large pyramidal neurons of IIIc are less prominent and yet form a more continuous band than in area 32 layer IIIc. Layers V and VI in area 14 are prominent, and they can be distinguished due to a clear and wide layer Vc.

Area 25. This area is the most caudal region in the subgenual mPFC. The key architectonic feature is its bilaminar appearance due to the prominent layers III and V-VI and a narrow layer IV (Fig. 3, K/L). Layer II neurons form isolated aggregates and an irregular and poorly differentiated border with layer III. Layer V has densely stained neurons, closely packed, and with no clear boundary with layer VI. A narrow layer IV together with the prominent bilaminar appearance can distinguish area 25 from area 14.

Two-dimensional unfolded maps

The two-dimensional maps of the mPFC showed that despite the variable size and shape of the sulci and gyri, the *pcs*, *cs*, and *srs* were the sulci that were most consistently associated with the mPFC subareal boundaries (Fig. 4). Neither the *irs* nor the *apos* were related to any particular boundary in our cases.

Sulci patterns in *ex vivo* brains

The mPFC sulci and gyri are the only identifiable anatomical references that can be used in MRI scans to identify the areal boundaries so far. The following three criteria were used to classify the sulci patterns of reference: a) presence/absence of *pcs*; b) position along the mPFC of *pcs* (i.e. rostral, dorsal and/or subgenual or all); c) connections (or not) of *cs* and *pcs* and with *srs*. According with these criteria, the 11 hemispheres could be classified within six different sulci patterns (Fig. 5A). As

illustrated in figure 5, sulci patterns 1 and 2 have *cs* but no *pcs*: In pattern 1, *cs* and *srs* are independent while in pattern 2 both are fused in a single sulcus. In 3 and 4, *pcs* is present and, together with *cs*, extends throughout the dorsal, rostral, and subgenual mPFC. The *cs* and *pcs* are separated from *srs* in 3, while in pattern 4 *pcs* joins *srs*. In patterns 5 and 6, *pcs* is present, but only dorsally. In 5, *cs* is independent of *srs* while in 6 *cs* joins *srs*.

Sulci patterns in *in vivo* brains

The six patterns found in the *ex vivo* sample were found identically in the 102 *in vivo* right and left hemispheres. Patterns 1, 2, and 4 accumulated 78% of the cases, while 3, 5, and 6 were less frequent (see frequency histogram in figure 5B). However, an additional new pattern (pattern 7 in figure 5B) was found, with *cs* dorsally and both *cs* and *pcs* ventrally, whereby *pcs* joined *srs*, but it was the least frequent (2.9%). All the sulci patterns from the *in vivo* sample are illustrated in 3D cortical surface reconstructions in figure 5 (bottom panel). Sulci pattern frequencies were statistically similar in both hemispheres and the pattern in one hemisphere did not predict the contralateral one, suggesting no lateralization in sulci patterns in the mPFC.

Guidelines for manual segmentation of mPFC areas in MRI scans

The guidelines are described in the following paragraphs and illustrated through figures 6-8. Rostral and caudal boundaries of the mPFC areas with respect to the frontal pole are shown in figure 6 in percent out of the whole mPFC longitudinal axis (i.e. from the frontal pole to the caudal end of area 25) and in mm in Table 1. Mean PFC and mPFC volumes from both *in vivo* and *ex vivo* cases normalized for brain size and corrected for shrinkage (Table 3).

Area 32. Dorsal and ventral boundaries of the pregenual portion of area 32 can be traced forward from the corresponding caudal subdivisions (Fig. 6, upper panel). Area 32 dorsal to the cc forms a band of cortex wider rostrally but progressively narrower at more caudal levels. In the most rostral sector (i.e. 87% of the distance from cc-end of mPFC), its CSL is (mean± SEM) 31.61± 3.88 mm in coronal sections as measured from the adjacent area 24 dorsally towards areas 8/9. The next caudal 5% of area 32 extends dorsally 18.33± 2.75 mm from area 24. The most caudal sector represents 8% of this dorsal portion of area 32 and its CSL is 7.14± 1.06 mm from area 24. In the subgenual region, area 32 CSL is 24.73± 2.05 mm. The CSL of area 32 in its caudal 1.5 mm is 11.94± 1.66 mm.

Area 24. Like in area 32, the pregenual dorsal and ventral boundaries of area 24 are a continuation from the caudal ones. The CSL of dorsal area 24 remains constant (29.59 ± 1.61 mm) independently of the shape and size of the CG. However, the morphology of the CG is an important reference to guide visually the localization of area 24 dorsal boundary. The caudal limit of dorsal area 24 in this study was considered at the end of the mPFC (see methods). As illustrated in figure 7, we found four morphologies of the CG with different cortical lengths:

a) *Cingulate gyrus with cortical surface length 24.79± 2.35 mm (small).* In these cases, the length of area 24 surpasses that of the CG; i.e. CSL of area 24 divided by that of the CG results in an area 24 that surpasses CG in 36%. Therefore, area 24 extends dorsally beyond the *cs*/CG and its boundary with area 32 is located at the mid-point of the medial-to-lateral axis of the upper bank of the *cs* (Fig. 7A).

b) *Cingulate gyrus with cortical surface length of 31.25± 0.91 mm (medium).* In these cases area 24 occupies most of the total CSL of the CG (95%). Visually, the boundary with dorsal area 32 in these cases falls in the fundus of the *cs* (Fig. 7B).

c) *Cingulate gyrus without ics with cortical surface length of 32.53± 2.90 mm (large).* The boundary of area 24 in these cases is located at the point of highest convexity of the ventral bank of the *cs*, and occupies 91% of the CG (Fig. 7C).

d) *Cingulate gyrus with ics with cortical surface length of 38.20± 3.00 mm (large).* The CSL of area 24 is smaller than that of CG, thus, it occupies approximately 77%

of the total CG. The boundary is placed at the point of the highest convexity of the dorsal bank of *ics* (Fig. 7D).

Like in the dorsal aspect of this area, the CG shape and size are independent of the CSL of area 24 (CS= 9.50± 0.89 mm). The caudal limit of subgenual area 24 extends 65.75± 3.65 mm from the frontal pole; 88.90± 2.68% of the total mPFC longitudinal axis (Fig. 7B).

a) *Cingulate gyrus with a cortical surface length of 16.99± 1.61 mm (large).* Area 24 boundary lays at the point of maximum convexity of the subgenual CG (Fig. 7E).

b) *Cingulate gyrus with cortical surface length of 9.83± 1.37 mm (small).* Area 24 boundary falls in the fundus of the ventral *cs* (Fig. 7F). The size of area 24 in the caudal 1.5 mm decreases to 5.63± 0.72 mm.

Area 14. The CSL of area 14 was 24.33± 2.00 mm in the first most rostral section, while for the remaining sections, CSL was 41.66± 3.00 mm (Fig. 6C). The boundary between area 14 and the OBFC is placed two-thirds from the gyrus rectus ventral tip to the olfactory sulcus. The boundary between area 14 and the subgenual area 32 depends mainly on whether there is junction between the *cs* and *srs* or not (Fig. 8A and B). When the *srs* is independent from the *cs* (patterns 1, 3, and 5), the boundary is at the fundus of the *srs* (Fig. 8A). Furthermore, if the *cs* (or *pcs*) and the *srs* join (patterns 2, 4, 6, and 7), this boundary corresponds to the point of highest convexity of the ventral bank of the *srs* (Fig. 8B).

Area 25. Area 25 CSL was 47.11± 2.35 mm, except for the last 1.5 mm where CSL decreases to 32.17± 1.66 mm. The boundary with the OBFC is the same as in the case of area 14 (Fig. 6C).

Probability maps

Continuous probability maps (Fig. 9) encode the probability of a given voxel of being part of mPFC areas 32, 24, 14, and 25 (Fig. 9A-D respectively), ranging from the minimum to the maximum coincidence (10 to 100%). This range expresses quantitatively the intersubject variability of a given architectonic subarea in an average

template brain. In the maximum probability map, a given voxel of each mPFC area gets the value of the area assigned with the highest probability for this position. Both types of maps are available in 1 and 2 mm MNI space.

DISCUSSION

The aims of this study are illustrated by the main findings: first, the creation of a set of quantitative and visual guidelines for segmentation of the areas 32, 24, 14, and 25 in MRI scans based on architectural analysis of histological material and sulci (*pcs, cs* and *srs*); second, probabilistic maps of the mPFC areas transferred to MNI space that can be used for region of interest (ROI)-functional/structural MRI group analysis. This study contributes to the progress from manual to probabilistic segmentation in MRI of mPFC areas. We now address some of the key issues on mPFC segmentation.

Disagreement in anatomical boundaries

The cytoarchitectonic subdivisions of the frontal lobe in general (Cox et al., 2014), and of mPFC in particular, have been a matter of debate due to the distinct parcellations made by different authors. Discrepancies exist not only within human studies but also in monkey cytoarchitectonic maps. Some previous comparative studies within the frontal lobe have tried to solved this problem, but they have been focused mainly in the dorsolateral (Petrides and Pandya, 1999) (areas 8, 9, and 46), ventrolateral areas 47 and 12 (Petrides and Pandya, 2002) and orbitofrontal regions (Ongür and Price, 2000), as well as in area 10 of the frontal pole (Semendeferi et al., 2001). The medial areas of the frontal lobe have been less thoroughly described. To help address this issue, the areas of the mPFC included in this study are labelled and described according to previous studies of human and rhesus monkey (Barbas and Pandya, 1989; Palomero-Gallagher et al., 2008). Doing this should make it easier to use information from tracing studies in monkeys to extrapolate anatomical and functional connectivity in humans in this region. However, and apart from its larger size in humans, the mPFC seems to have special anatomical features that complicate comparisons between species. One of the most relevant differences is in area 32 that, in non-human primates, is mostly restricted to the pregenual and subgenual regions, whereas in humans it has expanded dorsally to the

corpus callosum. This is an important point to be taken into account when connectivity patterns observed in primates are used to interpret connectivity analyses in humans.

Areas 24 and 32 have been a particular focus of discussion in terms of parcellation in humans. Both, area 24 (Petersen et al., 1988; Pardo et al., 1990; Jones et al., 1991; Talbot et al., 1991; Petit et al., 1993; Casey et al., 1994; Schlaug et al., 1994) and area 32 (Phan et al., 2002; Vogt et al., 2003) have been described as having at least two large subregions, one that extends rostral and dorsal to the corpus callosum and another one extending ventrally. These subregions appear to correlate with functional differences, i.e. the dorsal subfields are important in cognitive executive functions whereas more ventral subfields are more involved in affective processing (Bush et al., 2000). In our study, we have also identified the dorsal and subgenual divisions of areas 24 and 32. However, the architectonic differences between dorsal and ventral subdivisions of areas 24 and 32 were smaller than the similarities, and therefore, we did not subdivide area 24 and 32 any further in this study.

Segmentation of mPFC in MRI scans

The parcellations of the mPFC in histological sections and MRI scans have been restricted so far to the subgenual region including areas 24, 32, and 25 (Palomero-Gallagher et al., 2008; Palomero-Gallagher et al., 2009; Mackey and Petrides, 2014) in terms of cytoarchitectonic (Palomero-Gallagher et al., 2008) and receptor characteristics (Palomero-Gallagher et al., 2009). The results from these studies show cytoarchitectonic features that are, in general, in good agreement with our own results, with the exception of areas 33 and 14. Although we are aware of the distinctive features of area 33, we have purposely kept area 33 together with either area 24 or area 25 in our segmentation due to the difficulty in identifying this region reliably in MRI scans.

Recent studies have tried to correlate boundaries within the subgenual region with the most constant sulci (Mackey and Petrides, 2014; Palomero-Gallagher et al., 2015). Our mPFC parcellation is in line with these studies, although with some differences in the precise definition of the architectonic boundaries. In regard to the subgenual part of area 24, Palomero-Gallagher et al. (2015) placed the boundary with area 32 in the fundus of the cingulate sulcus or in the superior rostral gyrus, especially in the most caudal part.

By contrast, in our study, area 24 is more restricted and extends as far as the fundus of the cingulate sulcus at most, but never reaches the superior rostral gyrus. This result is in agreement with Mackey and Petrides (2014). With regard to area 25, Palomero-Gallagher et al. (2015) reports its rostral boundary at the fundus of the anterior parolfactory sulcus in 16 of the 20 hemispheres analysed. In the present study, we have established this limit more rostrally and our results indicate that the anterior parolfactory sulcus is not related with any architectonic boundary. Given that the cytoarchitectonic description of the mPFC areas are similarly described in all three studies, the differences found in the precise anatomical location of boundaries is likely be due to the different methods used to delineate them: while we used a classical visual microscopically assessment, Palomero-Gallagher et al. (2009) and Mackey and Petrides (2014), employed algorithm-based methods. In these studies, areal boundaries are established visually and then evaluated by digitalizing the stained sections and quantifying laminar changes in grey level indexes as an estimate of cellular density. This method gives a measurement of the degree of dissimilarity between adjacent groups of laminar profiles and allows establishing the borders between the areas, which makes the technique, in principle, more objective and reproducible. However, quantitative methods are not free of difficulties and their use not always gives replicable results, showing differences between studies of a similar magnitude that the ones shown by traditional architectonic parcellations (see Palomero-Gallagher et al., 2009; Mackey and Petrides, 2014). Therefore, further research is required to tease apart discrepancies like this, unlikely resolvable only with mere anatomical methods.

Sulci

Sulci and gyri morphology rather than cytoarchitectonic features are, of course, of special significance for MRI studies, especially for the development of tools for automatic segmentation (Xie et al., 2014).

Data on size and shape of brain sulci, as measured by gyrification index (GI), shows that although there are changes in embriogycal and early postnatal development, GI appear to stabilize by the age of 3/4, when gyri features appear remain relatively stable during adulthood (Zilles et al., 2013). This is in agreement with our own data, where

even though the age range of the *ex vivo* brains is wide, sulci remained stable as well as their relationship with architectonic boundaries.

We found that the most consistent sulci on the medial surface of the prefrontal cortex were the cingulate, intracingulate, paracingulate, superior rostral, inferior rostral, and anterior parolfactory sulci. These results are in agreement with Ono et al., (Ono et al., 1990), who described the frequency of the different patterns and confluences of the most consistent sulci in the whole brain, including the mPFC, in a sample of twenty-five *ex vivo* brains. Although the overall sulci appearance and variability in our study is in line with that reported by Ono, the sulcal patterns here have been defined and classified following the criteria of consistent anatomical association with mPFC areal boundaries; i.e. cingulate, paracingulate, and superior rostral sulci, and therefore, our results on frequencies are not comparable from the description provided by Ono et al., (1990).

Although the general anatomy of sulci has been properly studied, there is still relatively little information about their anatomical/genetic association with cytoarchitectonic boundaries in the adult brain or during development. Apart from the important and still uncertain developmental issue, the impact that different sulci patterns could have in terms of functional studies are yet to be fully appreciated. There are some studies reporting that, for example, the variability in the paracingulate sulcus could affect different aspects in cortex organization, including functional aspects in healthy and clinical populations (Vogt et al., 1995; Paus et al., 1996; Crosson et al., 1999; Fornito et al., 2004; Fornito et al., 2006). In our study, the paracingulate sulcus is the most variable sulcus along its longitudinal axis; this can make even the decision of its presence or absence somewhat subjective. For consistency, we considered this sulcus as present when the segment that runs around the genu of the corpus callosum was continuous. However, the sulci variability in normal healthy subjects makes it difficult to address this issue, and sulci mapping seems to be essential to understand the implications of the different cortical folding (Thompson et al., 1996). Due to this variability, there is also controversy about whether sulci can be consistently related with areal boundaries or not. Some studies have shown that an estimation of cortical areas on the basis of sulcal and gyral pattern is the best possible approximation at the present time (Fischl et al., 2008), and they have been previously used to delineate subareas in some regions such as the entorhinal cortex (Insausti et al., 1995; Insausti et al., 1998). In

contrast, others support that the high individual variability in terms of distances and depths makes difficult to create general rules to define landmarks based on these anatomical features and that probabilistic maps are essential (Zilles et al., 1997; Amunts et al., 2007). In our study, we opted for the combination of sulci patterns with the measurements of cortical surface length and distances, and thus far, they can be considered as reliable anatomical guidelines for MRI scans. To supplement these individual-specific guidelines, we have also created probabilistic maps in order to quantify the variability in the location of the subareas between subjects and show the most reliable regions within each area. These probabilistic maps could be used in MNI space as references to delineate regions of interest in studies involving mPFC. However, and in view of all these controversies involving the possible functional implications of sulci and gyri patterns, more investigation in this field is required.

Myelination

Gallyas' staining was used to confirm the boundaries between areas as established with Nissl stain. However, due to the poor myelinisation of the cortical grey matter in mPFC, this staining was only useful to confirm some boundaries, such as the one between dorsal areas 24 and 32, and the boundary of area 32 with the adjacent dorsomedial areas 9 and 8. This is in agreement with some recent studies which propose that the low myelin content in high order cognitive areas can be related with the intra-cortical plasticity, being the most plastic regions the ones with less myelin/volume (Glasser et al., 2014). According to this statement, higher association areas such as the limbic mPFC would require more plasticity and, therefore, less myelinisation than, for example, sensory areas. However, this is a working hypothesis that calls for further research.

Automatic segmentation

Automatic segmentation (or parcellation) of the cerebral cortex has been an important goal for many years and several automated and semi-automated tools have been developed with this aim. This work has provided masks that are nowadays available in 'standard space' in widely used programs like FSL or SPM. However, while these methods are starting to reach acceptable anatomical accuracy, and hence, reliability in

well-studied structures such as the hippocampus (Yushkevich et al., 2015), individual differences in brain morphology, size, orientation, or geometric complexity remain important problems when segmenting elsewhere in the cortex. There are also some technical issues that lead to heterogeneous segmentations between studies as in the use of different software tools, or differences in some MRI parameters such as sequences, signal-to-noise ratios, or image resolution (Geuze et al., 2005; Cox et al., 2014). That is why manual segmentation is still considered the *gold standard*, even though it is time-consuming. To ensure the least bias possible in our manual segmentations in terms of white matter and cerebral cortex boundaries, all MRI scans were pre-processed to obtain automatic parcellations of the whole prefrontal cortex before applying our manual segmentation of mPFC areas. This pre-processing steps addressed two critical issues: first MRI signal inhomogeneity; second, signal-to-noise ratio. Segmentation of the mPFC areas was only applied once the cortex-white matter boundaries were automatically segmented in all cases. Our protocol for manual segmentation of this region takes into account the inter-subject variability and provides visual guidelines and measurements to define the boundaries between areas in each subject. Although probabilistic maps of the mPFC were generated successfully, more research is needed to develop a fully automated protocol.

CONCLUSIONS

The mPFC has been associated with memory processing and consolidation due to its anatomical and functional connectivity with the limbic system. Many other higher order cognitive functions have, however, been considered in relation to the mPFC as well. The accurate anatomical parcellation provided in this study will be valuable for functional, structural, and molecular studies, as well as for understanding variations in healthy subjects and providing the basis for discriminant analysis in patient populations. This study provides architectonic-based quantitative and visual guidelines for mPFC segmentation in MRI scans as well as probabilistic maps useful for neuroimaging analyses as well as *ex vivo* molecular studies.

REFERENCES

Amunts K, Kedo O, Kindler M, Pieperhoff P, Mohlberg H, Shah NJ, Habel U, Schneider F, Zilles K (2005): Cytoarchitectonic mapping of the human amygdala, hippocampal region

and entorhinal cortex: intersubject variability and probability maps. Anat Embryol 210:343–352.

Amunts K, Schleicher A, Bürgel U, Mohlberg H, Uylings HB, Zilles K (1999): Broca's region revisited: cytoarchitecture and intersubject variability. J Comp Neurol 412:319–341.

Amunts K, Schleicher A, Zilles K (2007): Cytoarchitecture of the cerebral cortex--more than localization. Neuroimage 37:1061–1065; discussion 1066–1068.

Ashburner J, Friston KJ (2000): Voxel-based morphometry--the methods. Neuroimage 11:805–821.

Avants BB, Epstein CL, Grossman M, Gee JC (2008): Symmetric diffeomorphic image registration with cross-correlation: evaluating automated labeling of elderly and neurodegenerative brain. Med Image Anal 12:26–41.

Avants BB, Yushkevich P, Pluta J, Minkoff D, Korczykowski M, Detre J, Gee JC (2010): The optimal template effect in hippocampus studies of diseased populations. Neuroimage 49:2457–2466.

Barbas H (1992): Architecture and cortical connections of the prefrontal cortex in the rhesus monkey. Adv Neurol 57:91–115.

Barbas H, Pandya DN (1989): Architecture and intrinsic connections of the prefrontal cortex in the rhesus monkey. J Comp Neurol 286:353–375.

Bush G, Luu P, Posner M (2000): Cognitive and emotional influences in anterior cingulate cortex. Trends Cogn Sci (Regul Ed) 4:215–222.

Casey KL, Minoshima S, Berger KL, Koeppe RA, Morrow TJ, Frey KA (1994): Positron emission tomographic analysis of cerebral structures activated specifically by repetitive noxious heat stimuli. J Neurophysiol 71:802–807.

Cox RW (1996): AFNI: software for analysis and visualization of functional magnetic resonance neuroimages. Comput Biomed Res 29:162–173.

Cox SR, Ferguson KJ, Royle NA, Shenkin SD, MacPherson SE, MacLullich AMJ, Deary IJ, Wardlaw JM (2014): A systematic review of brain frontal lobe parcellation techniques in magnetic resonance imaging. Brain Struct Funct 219:1–22.

Crespo-Facorro B, Kim J, Andreasen NC, Spinks R, O'Leary DS, Bockholt HJ, Harris G, Magnotta VA (2000): Cerebral cortex: a topographic segmentation method using magnetic resonance imaging. Psychiatry Res 100:97–126.

Crosson B, Sadek JR, Bobholz JA, Gökçay D, Mohr CM, Leonard CM, Maron L, Auerbach EJ, Browd SR, Freeman AJ, Briggs RW (1999): Activity in the paracingulate and cingulate sulci during word generation: an fMRI study of functional anatomy. Cereb Cortex 9:307–316.

Dale AM, Fischl B, Sereno MI (1999): Cortical surface-based analysis. I. Segmentation and surface reconstruction. Neuroimage 9:179–194.

Desikan RS, Ségonne F, Fischl B, Quinn BT, Dickerson BC, Blacker D, Buckner RL, Dale AM, Maguire RP, Hyman BT, Albert MS, Killiany RJ (2006): An automated labeling system for subdividing the human cerebral cortex on MRI scans into gyral based regions of interest. Neuroimage 31:968–980.

Destrieux C, Fischl B, Dale A, Halgren E (2010): Automatic parcellation of human cortical gyri and sulci using standard anatomical nomenclature. Neuroimage 53:1–15.

Fischl B, Liu A, Dale AM (2001): Automated manifold surgery: constructing geometrically accurate and topologically correct models of the human cerebral cortex. IEEE Trans Med Imaging 20:70–80.

Fischl B, Rajendran N, Busa E, Augustinack J, Hinds O, Yeo BTT, Mohlberg H, Amunts K, Zilles K (2008): Cortical folding patterns and predicting cytoarchitecture. Cereb Cortex 18:1973–1980.

Fischl B, Salat DH, Busa E, Albert M, Dieterich M, Haselgrove C, Van der Kouwe A, Killiany R, Kennedy D, Klaveness S, Montillo A, Makris N, Rosen B, Dale AM (2002): Whole brain segmentation: automated labeling of neuroanatomical structures in the human brain. Neuron 33:341-55.

Fischl B, Sereno MI, Dale AM (1999): Cortical surface-based analysis. II: Inflation, flattening, and a surface-based coordinate system. Neuroimage 9:195–207.

Fonov VS, Evans AC, McKinstry RC, Almli CR Collins DL (2004): Unbiased nonlinear average age-appropriate brain templates from birth to adulthood. NeuroImage 47:S102

Fornito A, Yücel M, Wood S, Stuart GW, Buchanan JA, Proffitt T, Anderson V, Velakoulis D, Pantelis C (2004): Individual differences in anterior cingulate/paracingulate morphology are related to executive functions in healthy males. Cereb Cortex 14:424–431.

Fornito A, Whittle S, Wood SJ, Velakoulis D, Pantelis C, Yücel M (2006): The influence of sulcal variability on morphometry of the human anterior cingulate and paracingulate cortex. Neuroimage 33:843–854.

Gadian DG, Aicardi J, Watkins KE, Porter DA, Mishkin M, Vargha-Khadem F (2000): Developmental amnesia associated with early hypoxic-ischaemic injury. Brain 123:499-507.

Gallyas F (1971): A principle for silver staining of tissue elements by physical development. Acta Morphol Acad Sci Hung 19:57–71.

Geuze E, Vermetten E, Bremner JD (2005): MR-based in vivo hippocampal volumetrics: 1. Review of methodologies currently employed. Mol Psychiatry 10:147–159.

Glasser MF, Goyal MS, Preuss TM, Raichle ME, Van Essen DC (2014): Trends and properties of human cerebral cortex: correlations with cortical myelin content. Neuroimage 93:165–175.

Goulas A, Uylings HBM, Stiers P (2012): Unravelling the intrinsic functional organization of the human lateral frontal cortex: A parcellation scheme based on resting state fMRI. J Neurosci 32:10238–10252.

Insausti R, Juottonen K, Soininen H, Insausti AM, Partanen K, Vainio P, Laakso MP, Pitkänen A (1998): MR volumetric analysis of the human entorhinal, perirhinal, and temporopolar cortices. AJNR Am J Neuroradiol 19:659–671.

Insausti R, Tuñón T, Sobreviela T, Insausti AM, Gonzalo LM (1995): The human entorhinal cortex: a cytoarchitectonic analysis. J Comp Neurol 355:171–198.

Jones AK, Brown WD, Friston KJ, Qi LY, Frackowiak RS (1991): Cortical and subcortical localization of response to pain in man using positron emission tomography. Proc Biol Sci 244:39–44.

Klein A, Tourville J (2012): 101 Labeled brain images and a consistent human cortical Labeling protocol. Front Neurosci 6:171.

Lancaster JL, Rainey LH, Summerlin JL, Freitas CS, Fox PT, Evans AC, Toga AW, Mazziotta JC (1997): Automated labeling of the human brain: a preliminary report on the development and evaluation of a forward-transform method. Hum Brain Mapp 5:238–242.

Lancaster JL, Woldorff MG, Parsons LM, Liotti M, Freitas CS, Rainey L, Kochunov PV, Nickerson D, Mikiten SA, Fox PT (2000): Automated Talairach atlas labels for functional brain mapping. Hum Brain Mapp 10:120–131.

Mackey S, Petrides M (2014): Architecture and morphology of the human ventromedial prefrontal cortex. Eur J Neurosci 40:2777–2796.

Mai JK, Majtanik M, Paxinos G (2015): Atlas of the Human Brain, 4th Edition. Academic Press.

Morecraft RJ, Stilwell-Morecraft KS, Cipolloni PB, Ge J, McNeal DW, Pandya DN (2012): Cytoarchitecture and cortical connections of the anterior cingulate and adjacent somatomotor fields in the rhesus monkey. Brain Res Bull 87:457–497.

Ongür D, Price JL (2000): The organization of networks within the orbital and medial prefrontal cortex of rats, monkeys and humans. Cereb Cortex 10:206–219.

Ono M, Kubik S, Abernathey CD (1990): Atlas of the Cerebral Sulci. Thieme.

Palomero-Gallagher N, Eickhoff SB, Hoffstaedter F, Schleicher A, Mohlberg H, Vogt BA, Amunts K, Zilles K (2015): Functional organization of human subgenual cortical areas: Relationship between architectonical segregation and connectional heterogeneity. Neuroimage 115:177–190.

Palomero-Gallagher N, Mohlberg H, Zilles K, Vogt B (2008): Cytology and receptor architecture of human anterior cingulate cortex. J Comp Neurol 508:906–926.

Palomero-Gallagher N, Vogt BA, Schleicher A, Mayberg HS, Zilles K (2009): Receptor architecture of human cingulate cortex: Evaluation of the four-region neurobiological model. Hum Brain Mapp 30:2336–2355.

Pardo JV, Pardo PJ, Janer KW, Raichle ME (1990): The anterior cingulate cortex mediates processing selection in the Stroop attentional conflict paradigm. Proc Natl Acad Sci U S A 87:256–259.

Paus T, Otaky N, Caramanos Z, MacDonald D, Zijdenbos A, D'Avirro D, Gutmans D, Holmes C, Tomaiuolo F, Evans AC (1996): In vivo morphometry of the intrasulcal gray matter in the human cingulate, paracingulate, and superior-rostral sulci: hemispheric asymmetries, gender differences and probability maps. J Comp Neurol 376:664–673.

Petersen SE, Fox PT, Posner MI, Mintun M, Raichle ME (1988): Positron emission tomographic studies of the cortical anatomy of single-word processing. Nature 331:585–589.

Petit L, Orssaud C, Tzourio N, Salamon G, Mazoyer B, Berthoz A (1993): PET study of voluntary saccadic eye movements in humans: basal ganglia-thalamocortical system and cingulate cortex involvement. J Neurophysiol 69:1009–1017.

Petrides M (2012): The human cerebral cortex: An MRI atlas of the sulci and gyri in MNI stereotaxic space 1 edition. London ; Waltham, MA: Academic Press.

Petrides M, Pandya DN (1999): Dorsolateral prefrontal cortex: comparative cytoarchitectonic analysis in the human and the macaque brain and corticocortical connection patterns. Eur J Neurosci 11:1011–1036.

Petrides M, Pandya DN (2002): Comparative cytoarchitectonic analysis of the human and the macaque ventrolateral prefrontal cortex and corticocortical connection patterns in the monkey. Eur J Neurosci 16:291–310.

Phan KL, Wager T, Taylor SF, Liberzon I (2002): Functional neuroanatomy of emotion: A meta-analysis of emotion activation studies in PET and fMRI. NeuroImage 16:331–348.

Rademacher J, Morosan P, Schormann T, Schleicher A, Werner C, Freund HJ, Zilles K (2001): Probabilistic mapping and volume measurement of human primary auditory cortex. Neuroimage 13:669–683.

Rajkowska G, Goldman-Rakic PS (1995): Cytoarchitectonic definition of prefrontal areas in the normal human cortex: II. Variability in locations of areas 9 and 46 and relationship to the Talairach Coordinate System. Cereb Cortex 5:323–337.

Roland P, Svensson G, Lindeberg T, Risch T, Baumann P, Dehmel A, Frederiksson J, Halldorson H, Forsberg L, Young J, Zilles K (2001): A database generator for human brain imaging. Trends Neurosci 24:562–564.

Schlaug G, Knorr U, Seitz R (1994): Inter-subject variability of cerebral activations in acquiring a motor skill: a study with positron emission tomography. Exp Brain Res 98:523–534.

Schneider CA, Rasband WS, Eliceiri KW (2012): NIH Image to ImageJ: 25 years of image analysis. Nat Meth 9:671–675.

Semendeferi K, Armstrong E, Schleicher A, Zilles K, Van Hoesen GW (2001): Prefrontal cortex in humans and apes: a comparative study of area 10. Am J Phys Anthropol 114:224–241.

Shattuck DW, Mirza M, Adisetiyo V, Hojatkashani C, Salamon G, Narr KL, Poldrack RA, Bilder RM, Toga AW (2008): Construction of a 3D probabilistic atlas of human cortical structures. Neuroimage 39:1064–1080.

Talairach J, Tournoux P (1988): Co-planar stereotaxic atlas of the human brain: 3-D dimensional proportional system: An approach to cerebral imaging. Trans. Mark Rayport. Stuttgart ; New York: Thieme Medical Publishers.

Talbot JD, Marrett S, Evans AC, Meyer E, Bushnell MC, Duncan GH (1991): Multiple representations of pain in human cerebral cortex. Science 251:1355–1358.

Thompson PM, Schwartz C, Lin RT, Khan AA, Toga AW (1996): Three-dimensional statistical analysis of sulcal variability in the human brain. J Neurosci 16:4261–4274.

Tzourio-Mazoyer N, Landeau B, Papathanassiou D, Crivello F, Etard O, Delcroix N, Mazoyer B, Joliot M (2002): Automated anatomical labeling of activations in SPM using a macroscopic anatomical parcellation of the MNI MRI single-subject brain. Neuroimage 15:273–289.

Van Essen DC (2002): Windows on the brain: the emerging role of atlases and databases in neuroscience. Curr Opin Neurobiol 12:574–579.

Van Essen DC, Maunsell JHR (1980): Two-Dimensional Maps of the Cerebral-Cortex. J Comp Neurol 191:255–281.

Vogt BA, Nimchinsky EA, Vogt LJ, Hof PR (1995): Human cingulate cortex: surface features, flat maps, and cytoarchitecture. J Comp Neurol 359:490–506.

Vogt BA, Berger GR, Derbyshire SWG (2003): Structural and functional dichotomy of human midcingulate cortex. Eur J Neurosci 18:3134–3144.

Von Economo C, Koskinas GN (2008) Atlas of cytoarchitectonics of the adult human cerebral cortex (trans, rev, ed: Triarhou LC). Karger, Basel.

Xie L, Pluta J, Wang H, Das SR, Mancuso L, Kliot D, Avants BB, Ding SL, Wolk DA, Yushkevich PA (2014): Automatic clustering and thickness measurement of anatomical variants of the human perirhinal cortex. In: Golland, P, Hata, N, Barillot, C, Hornegger, J, Howe, R, editors. Medical Image Computing and Computer-Assisted Intervention – MICCAI 2014. Springer International Publishing. Lecture Notes in Computer Science 8675 pp 81–88.

Yushkevich PA, Amaral RSC, Augustinack JC, Bender AR, Bernstein JD, Boccardi M, Bocchetta M, Burggren AC, Carr VA, Chakravarty MM, Chételat G, Daugherty AM, Davachi L, Ding SL, Ekstrom A, Geerlings MI, Hassan A, Huang Y, Iglesias J Eugenio, La Joie R, Kerchner GA, LaRocque KF, Libby LA, Malykhin N, Mueller SG, Olsen RK,

Palombo DJ, Parekh MB, Pluta JB, Preston AR, Pruessner JC, Ranganath C, Raz N, Schlichting ML, Schoemaker D, Singh S, Stark CEL, Suthana N, Tompary A, Turowski MM, Van LK, Wagner AD, Wang L, Winterburn Julie L, Wisse Laura E M, Yassa MA, Zeineh MM (2015): Quantitative comparison of 21 protocols for labeling hippocampal subfields and parahippocampal subregions in in vivo MRI: towards a harmonized segmentation protocol. NeuroImage 111:526-41.

Yushkevich PA, Piven J, Hazlett HC, Smith RG, Ho S, Gee JC, Gerig G (2006): User-guided 3D active contour segmentation of anatomical structures: significantly improved efficiency and reliability. Neuroimage 31:1116–1128.

Yushkevich PA, Pluta JB, Wang H, Xie L, Ding S-L, Gertje EC, Mancuso L, Kliot D, Das SR, Wolk DA (2015): Automated volumetry and regional thickness analysis of hippocampal subfields and medial temporal cortical structures in mild cognitive impairment. Hum Brain Mapp 36:258–287.

Zilles K, Palomero-Gallagher N, Amunts K (2013): Development of cortical folding during evolution and ontogeny. Trends Neurosci 36:275-84.

Zilles K, Schleicher A, Langemann C, Amunts K, Morosan P, Palomero-Gallagher N, Schormann T, Mohlberg H, Bürgel U, Steinmetz H, Schlaug G, Roland PE (1997): Quantitative analysis of sulci in the human cerebral cortex: development, regional heterogeneity, gender difference, asymmetry, intersubject variability and cortical architecture. Hum Brain Mapp 5:218–221.

Figure legends

Figure 1. Cytoarchitectonic areas found in the mPFC. Medial view of a human hemisphere illustrates the approximate location of the mPFC areas described in this study. The arrowheads indicate the sulci of reference. Abbreviations: *apos*, anterior parolfactory sulcus; *cs*, cingulate sulcus; *ics*, intracingulate suclus; *irs*, inferior rostral sulcus; *pcs*, paracingulate sulcus; *srs* superior rostral sulcus.

Figure 2. Schematic drawings of a medial view of the mPFC and coronal sections (1-13) through the frontal lobe illustrate the location of areas 32, 24, 14, and 25 of the mPFC. The vertical lines on the medial view indicate the approximate position of the coronal sections in the rostro-caudal axis. Abbreviations like in Figure 1. cc, corpus callosum; Cd, caudate nucleus.

Figure 3. Microphotographs of Nissl- and Gallyas-stained sections of areas 32 (A/B and E/F), 24 (C/D and G/H), 14 (I/J), and 25 (K/L) illustrate cortical layers (I-VI) and cyto- and myeloarchitectonic features of the mPFC subareas. Within areas 32 and 24, a dorsal (A/B and C/B, respectively) and a subgenual region can be distinguished (E/F and G/H, respectively). Scale bar: 250 µm.

Figure 4. Two-dimentional unfolded maps of the arechitectonic areas 32, 24, 14 and 25 of the mPFC included in this study. Cingulate and superior rostral sulci, highlighted with dashed lines, were the ones most consistently associated with boundaries in this study.

Figure 5. A. Medial views of human hemispheres illustrating the 6 sulci patterns found in the 11 *ex vivo* cases. **B**. Histogram shows the frequency of the 6 patterns found in the ex vivo cases *in vivo* samples with only one new pattern (7 inset) identified in the *in vivo* sample. This pattern 7 was the least frequent (grey bar). In pattern 7, *pcs* joins *srs* in the subgenual region (see inset on the right). Scale bar: 1cm. The histogram illustrates the frequency of occurrence (in percentage) of the 7 different sulci patterns found in the *in vivo* cases. **C.** Cortical surface reconstructions of the *in vivo* MRI scans illustrate the same 1-6 sulci patterns and the new pattern 7 found in the *in vivo* 51 MRI scans. Sulci are demarcated with dashed lines. Abbreviations as in previous figures.

Figure 6. Schematic drawings of brain hemispheres sagittal views and coronal sections through the frontal lobe (indicated by vertical numbered dashed lines) show the two types of measurements taken in the *ex vivo* hemispheres to guide the segmentation of the mPFC subareas in MRI scans. On the left, medial views of the brain show the distance from the frontal pole to the rostral and caudal limits of each mPFC subarea in percent of total length of mPFC (horizontal dashed lines). On the right, coronal sections show the mean cortical surface length (CSL, in mm +/- SEM) of the corresponding mPFC area. Note all the measurements are normalized for frontal cortex volume and tissue shrinkage. **A.** Area 32. **B.** Area 24. **C.** Areas 14 and 25.

Figure 7. Nissl stained coronal sections (top row) and MRI scans (bottom row) of area 24. The arrowheads indicate the boundaries of dorsal (A-D) and subgenual (E, F) parts of area 24 depending of the cingulate gyrus (CG) size. **A.** Small CG. **B.** Medium CG. **C.** Large CG. **D.** Large CG with *ics*. **E.** Small subgenual CG. **F.** Large subgenual CG. Abbreviations like in previous figures, lv, lateral ventricle.

Figure 8. Nissl stained coronal sections (top row) and MRI scans (bottom row) of area 14. The arrowheads indicate the boundaries between area 14 and subgenual area 32 and OBFC. **A.** Case in which *srs* is independent from *cs*. **B.** Case in which *srs* joins *cs*.

Figure 9A. Continuous probability map of area 32 for the right hemisphere in 51 MRI scans projected into the MNI average brain template. The probability of a voxel belonging to area 32 is illustrated in color-coded to percentage range (10-100%) with warmer colours for voxels with higher probabilities. **B.** Continuous probability map of area 24 for the right hemisphere in 51 MRI scans projected into the MNI average brain template. The probability of a voxel belonging to area 24 is illustrated in color-coded to percentage range (10-100%) with warmer colours for voxels with higher probabilities. **C.** Continuous probability map of area 14 for the right hemisphere in 51 MRI scans projected into the MNI average brain template. The probability of a voxel belonging to area 14 is illustrated in color-coded to percentage range (10-100%) with warmer colours for voxels with higher probabilities. **D.** Continuous probability map of area 25 for the right hemisphere in 51 MRI scans projected into the MNI average brain template. The probability of a voxel belonging to area 25 is illustrated in color-coded to percentage range (10-100%) with warmer colours for voxels with higher probabilities.

Table 1. Distance from the frontal pole to the rostral limit of the mPFC subareas in native space adjusted for ICV and shrinkage.

mPFC	*Distance from frontal pole (mm±sd)*
Area 32	
Pregenual	18.16± 1.30
Subgenual	60.93± 3.10
Area 24	
Pregenual	27.57± 1.50
Subgenual	65.75± 3.65
Area 14	17.63± 1.34
Area 25	53.21± 3.84

Table 2. Sulcal nomenclature used previously for the sulci located in mPFC.

Author (Year)	*Medial frontal sulci across studies*			
Present study	Superior rostral (srs)	Inferior rostral (irs)	Cingulate (cs)	Paracingulate (pcs)
Von Economo & Koskinas (1925)	rs	ri	Intralimbicus (I)	Callosomarginalis (cmg)
Ono et al., (1990)	srs	irs	cs	pcs
Paus et al., (1996)	irs	irs	cs	pcs
Petrides (2012)	ros, asos[2], sos[3]	irs	cgs	pcgs,
Mackey & Petrides (2014)	SRS, MPS[4]	IRS	CS	SupraRS[5] SCS
Palomero-Gallager et al., (2015)	srs	irs	cs	pcs

[1]There has been agreement across studies in the location of the anterior paraolfactory sulcus and, therefore, only differences in the abbreviations as stated in this table.
[2]Accessory supraorbital sulcus (asos), corresponds to a polar branch of srs in the present study
[4]Medial polar sulcus (MPS); corresponds to the rostral polar extension of srs in the present study.
[5]Supra rostral sulcus (SupraRS); corresponds with the subgenual branch of the paracingulate sulcus (pcs) in the present study.

Table 3. Mean PFC and mPFC volumes in *ex vivo* and *in vivo* MRI scans after corrected for brain size and tissue shrinkage.

	Ex vivo (n=11)		*In vivo* (n=102)	
Areas	Mean vol[1]±SEM	Mean %[2]±SEM	Mean vol±SEM	Mean %±SEM
PFC	72604.70± 4089.86	N/A	95156.86± 922.90	N/A
mPFC	11342.02± 701.48	15.30± 0.62	14913.76± 144.86	15.71± 0.10
32	5139.79± 303.37	6.93± 0.25	7336.28± 83.18	7.73± 0.07
24	2957.76± 173.62	3.99± 0.20	3630.79± 66.24	3.81± 0.06
14	2177.04± 262.98	2.94± 0.30	2526.41± 31.76	2.66± 0.03
25	1067.43± 95.69	1.43± 0.08	1420.29± 20.95	1.50± 0.02

[1]Volume is shown in mm^3.
[2]Percent of PFC volume.

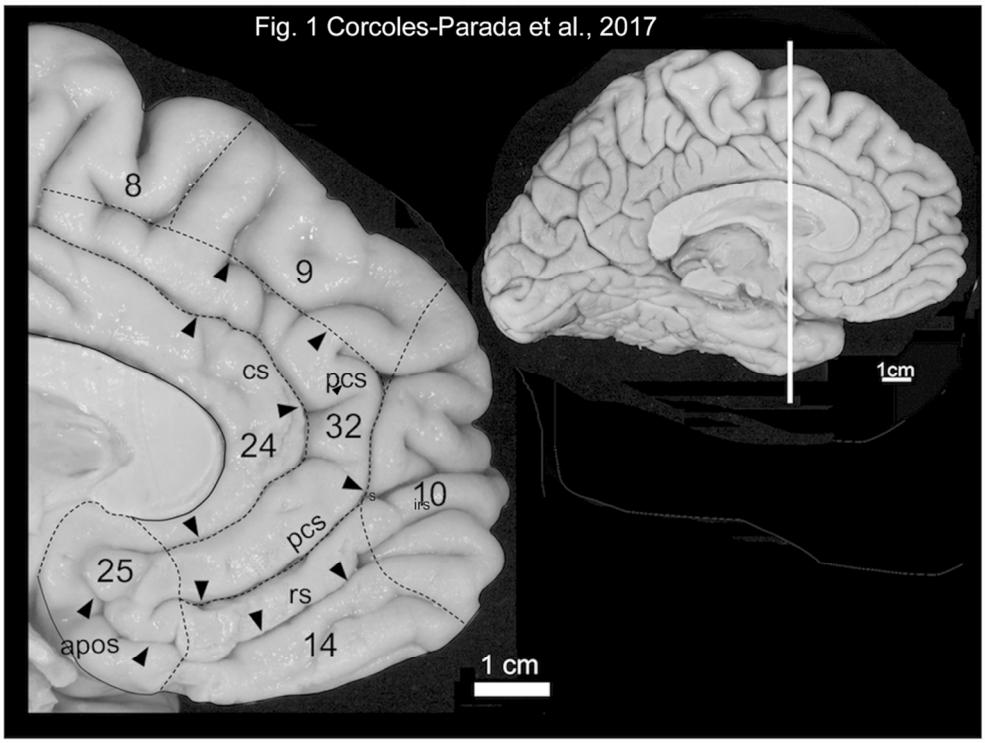

Figure 1. Cytoarchitectonic areas found in the mPFC. Medial view of a human hemisphere illustrates the approximate location of the mPFC areas described in this study. The arrowheads indicate the sulci of reference. Abbreviations: apos, anterior parolfactory sulcus; cs, cingulate sulcus; ics, intracingulate suclus; irs, inferior rostral sulcus; pcs, paracingulate sulcus; srs superior rostral sulcus.

102x77mm (300 x 300 DPI)

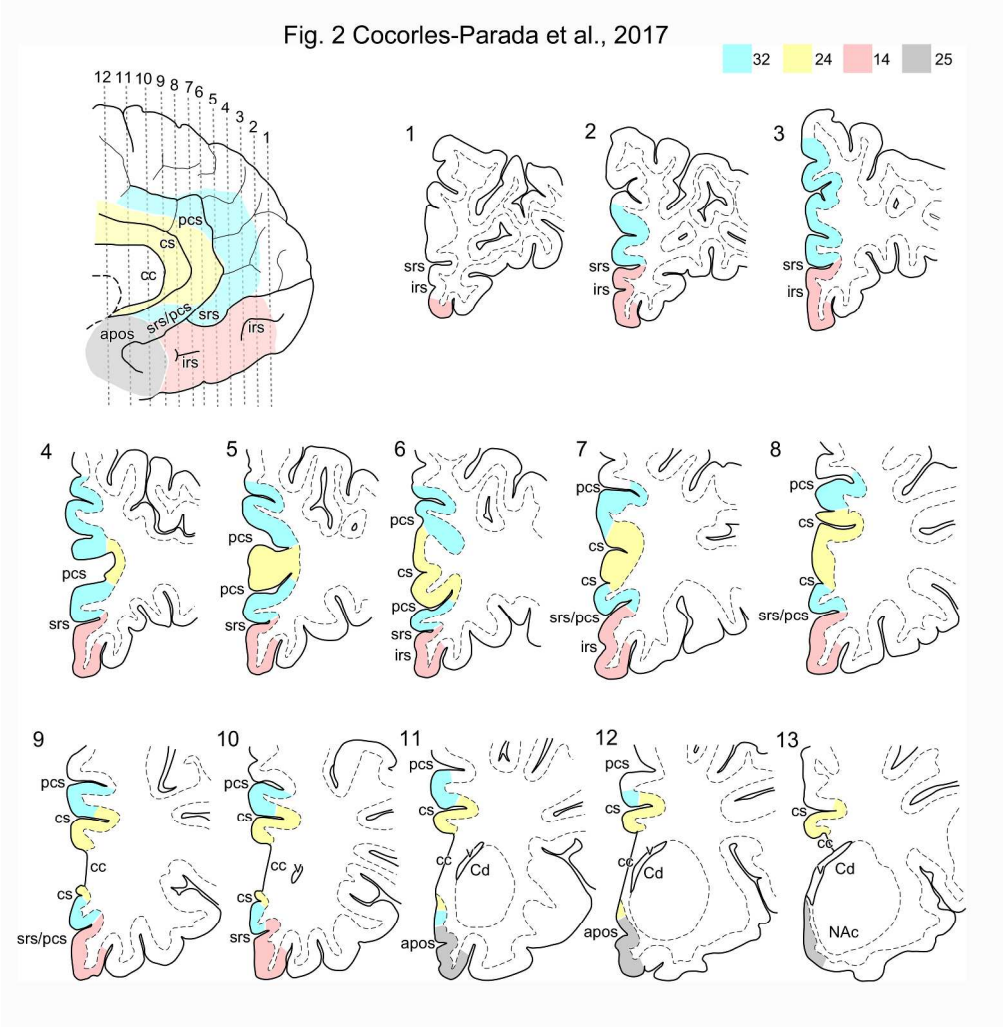

Figure 2. Schematic drawings of a medial view of the mPFC and coronal sections (1-13) through the frontal lobe illustrate the location of areas 32, 24, 14, and 25 of the mPFC. The vertical lines on the medial view indicate the approximate position of the coronal sections in the rostro-caudal axis. Abbreviations like in Figure 1. cc, corpus callosum; Cd, caudate nucleus. ‼ ┼

159x180mm (600 x 600 DPI)

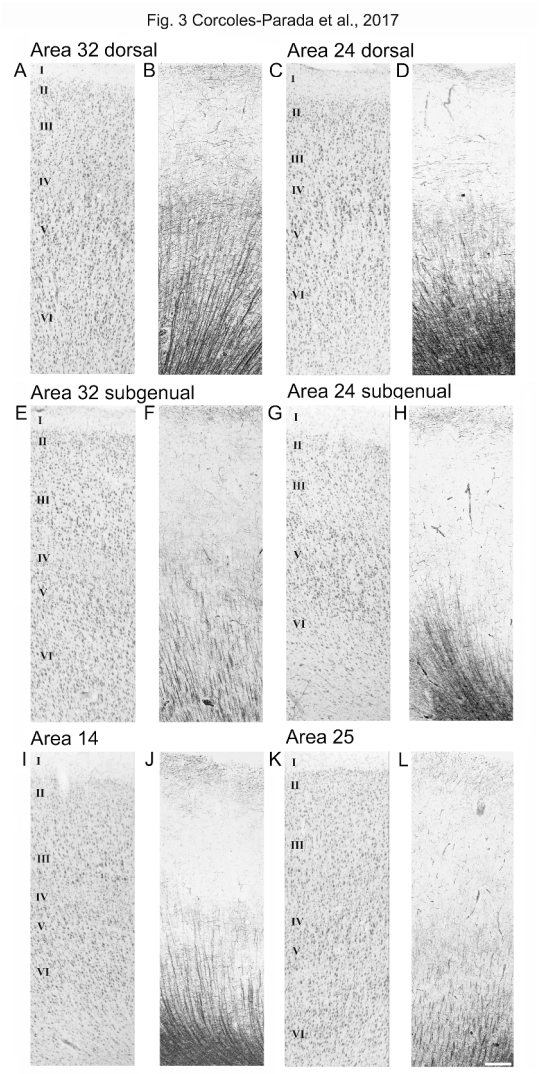

Figure 3. Microphotographs of Nissl- and Gallyas-stained sections of areas 32 (A/B and E/F), 24 (C/D and G/H), 14 (I/J), and 25 (K/L) illustrate cortical layers (I-VI) and cyto- and myeloarchitectonic features of the mPFC subareas. Within areas 32 and 24, a dorsal (A/B and C/B, respectively) and a subgenual region can be distinguished (E/F and G/H, respectively). Scale bar: 250 μm.‼ ┼

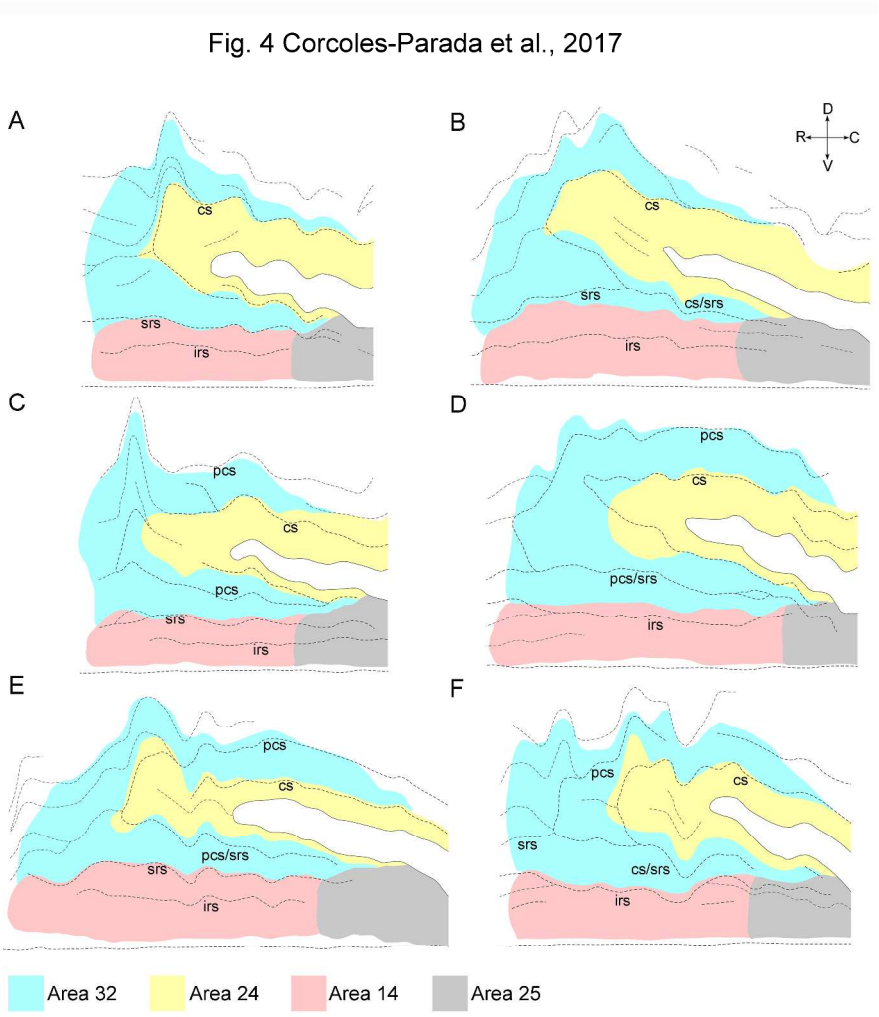

Figure 4. Two-dimentional unfolded maps of the arechitectonic areas 32, 24, 14 and 25 of the mPFC included in this study. Cingulate and superior rostral sulci, highlighted with dashed lines, were the ones most consistently associated with boundaries in this study. ‼ ┼

Fig. 5 Corcoles-Parada et al., 2017

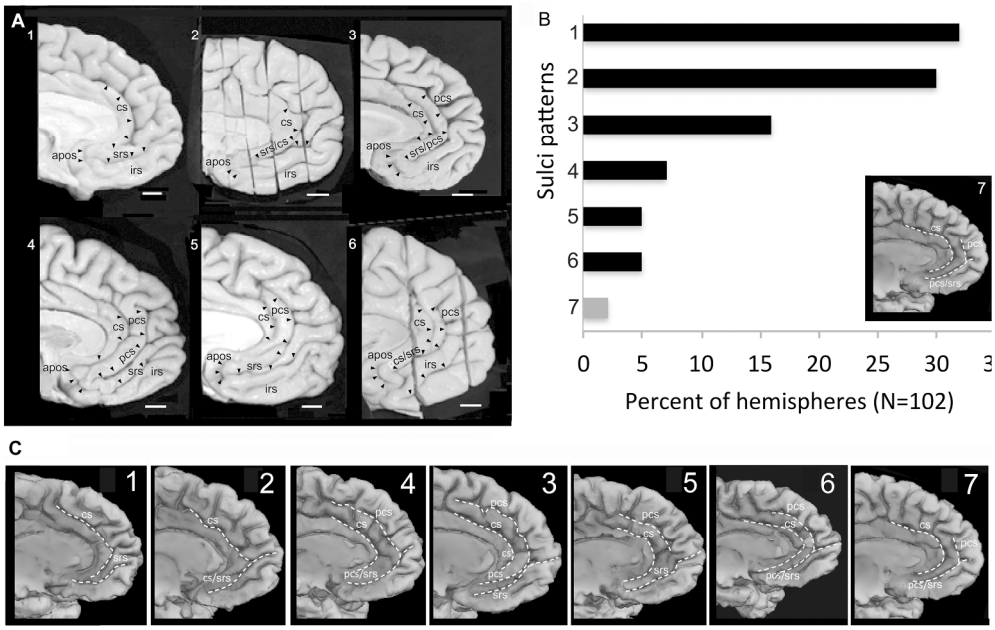

Figure 5. A. Medial views of human hemispheres illustrating the 6 sulci patterns found in the 11 ex vivo cases. B. Histogram shows the frequency of the 6 patterns found in the ex vivo cases in vivo samples with only one new pattern (7 inset) identified in the in vivo sample. This pattern 7 was the least frequent (grey bar). In pattern 7, pcs joins srs in the subgenual region (see inset on the right). Scale bar: 1cm. The histogram illustrates the frequency of occurrence (in percentage) of the 7 different sulci patterns found in the in vivo cases. C. Cortical surface reconstructions of the in vivo MRI scans illustrate the same 1-6 sulci patterns and the new pattern 7 found in the in vivo 51 MRI scans. Sulci are demarcated with dashed lines. Abbreviations as in previous figures.‼ ┼

113x91mm (600 x 600 DPI)

Fig. 6 Corcoles-Parada et al., 2017

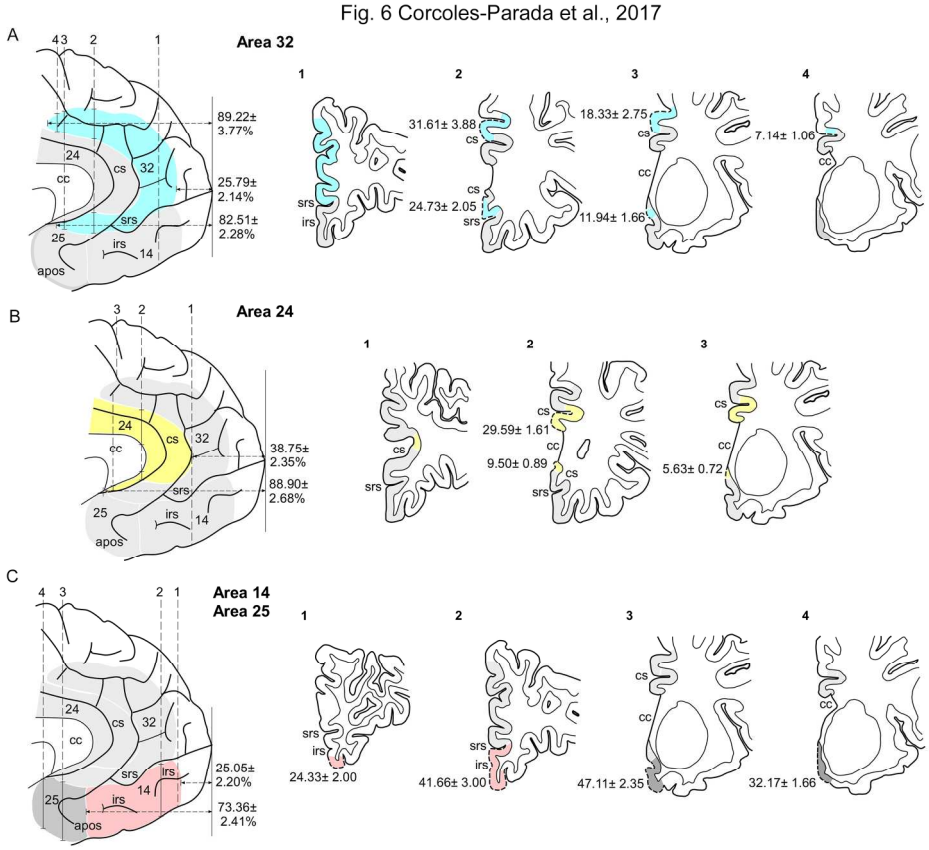

Figure 6. Schematic drawings of brain hemispheres sagittal views and coronal sections through the frontal lobe (indicated by vertical numbered dashed lines) show the two types of measurements taken in the ex vivo hemispheres to guide the segmentation of the mPFC subareas in MRI scans. On the left, medial views of the brain show the distance from the frontal pole to the rostral and caudal limits of each mPFC subarea in percent of total length of mPFC (horizontal dashed lines). On the right, coronal sections show the mean cortical surface length (CSL, in mm +/- SEM) of the corresponding mPFC area. Note all the measurements are normalized for frontal cortex volume and tissue shrinkage. A. Area 32. B. Area 24. C. Areas 14 and 25.
‼ ┼

194x185mm (300 x 300 DPI)

Fig. 7 Corcoles-Parada et al., 2017

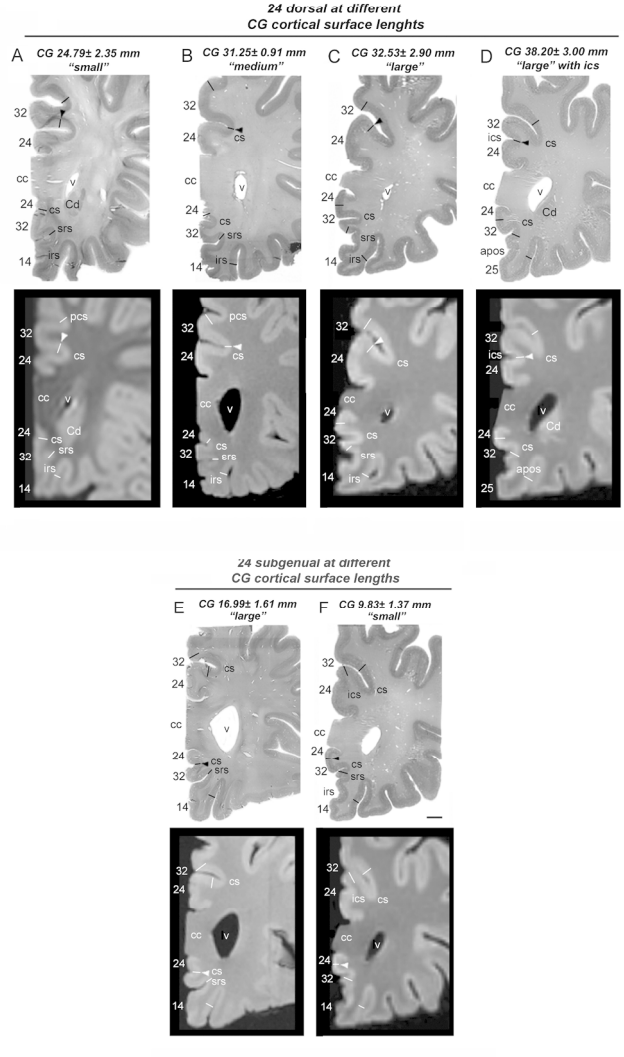

‼ ┼ Figure 7. Nissl stained coronal sections (top row) and MRI scans (bottom row) of area 24. The arrowheads indicate the boundaries of dorsal (A-D) and subgenual (E, F) parts of area 24 depending of the cingulate gyrus (CG) size. A. Small CG. B. Medium CG. C. Large CG. D. Large CG with ics. E. Small subgenual CG. F. Large subgenual CG. Abbreviations like in previous figures, lv, lateral ventricle.‼ ┼

Fig. 8 Corcoles-Parada et al., 2017

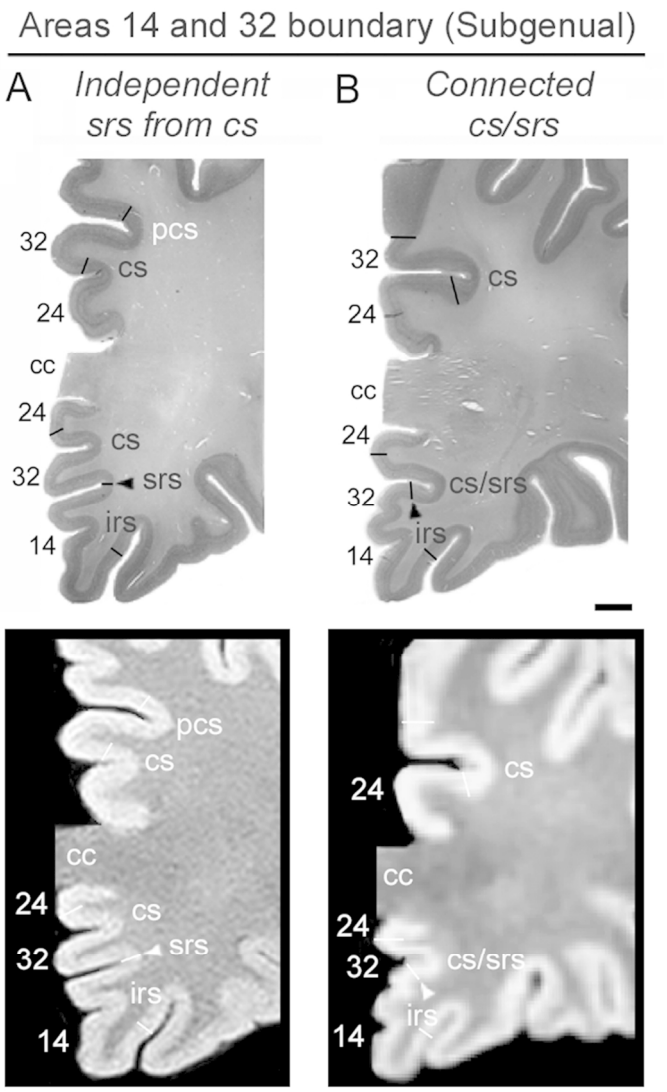

Figure 8. Nissl stained coronal sections (top row) and MRI scans (bottom row) of area 14. The arrowheads indicate the boundaries between area 14 and subgenual area 32 and OBFC. A. Case in which srs is independent from cs. B. Case in which srs joins cs.‼ ┼

Fig. 9A Corcoles-Parada et al., 2017

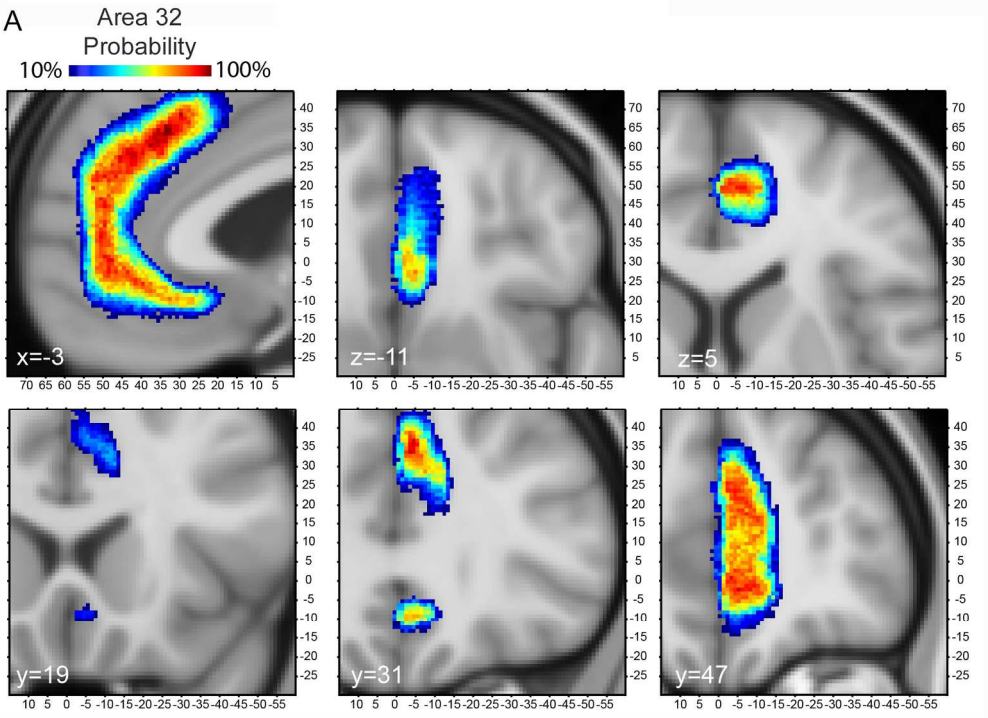

Figure 9A. Continuous probability map of area 32 for the right hemisphere in 51 MRI scans projected into the MNI average brain template. The probability of a voxel belonging to area 32 is illustrated in color-coded to percentage range (10-100%) with warmer colours for voxels with higher probabilities. B. Continuous probability map of area 24 for the right hemisphere in 51 MRI scans projected into the MNI average brain template. The probability of a voxel belonging to area 24 is illustrated in color-coded to percentage range (10-100%) with warmer colours for voxels with higher probabilities. C. Continuous probability map of area 14 for the right hemisphere in 51 MRI scans projected into the MNI average brain template. The probability of a voxel belonging to area 14 is illustrated in color-coded to percentage range (10-100%) with warmer colours for voxels with higher probabilities. D. Continuous probability map of area 25 for the right hemisphere in 51 MRI scans projected into the MNI average brain template. The probability of a voxel belonging to area 25 is illustrated in color-coded to percentage range (10-100%) with warmer colours for voxels with higher probabilities.‼ ┼ ‼ ┼

175x147mm (299 x 299 DPI)

Fig. 9B Corcoles-Parada et al., 2017

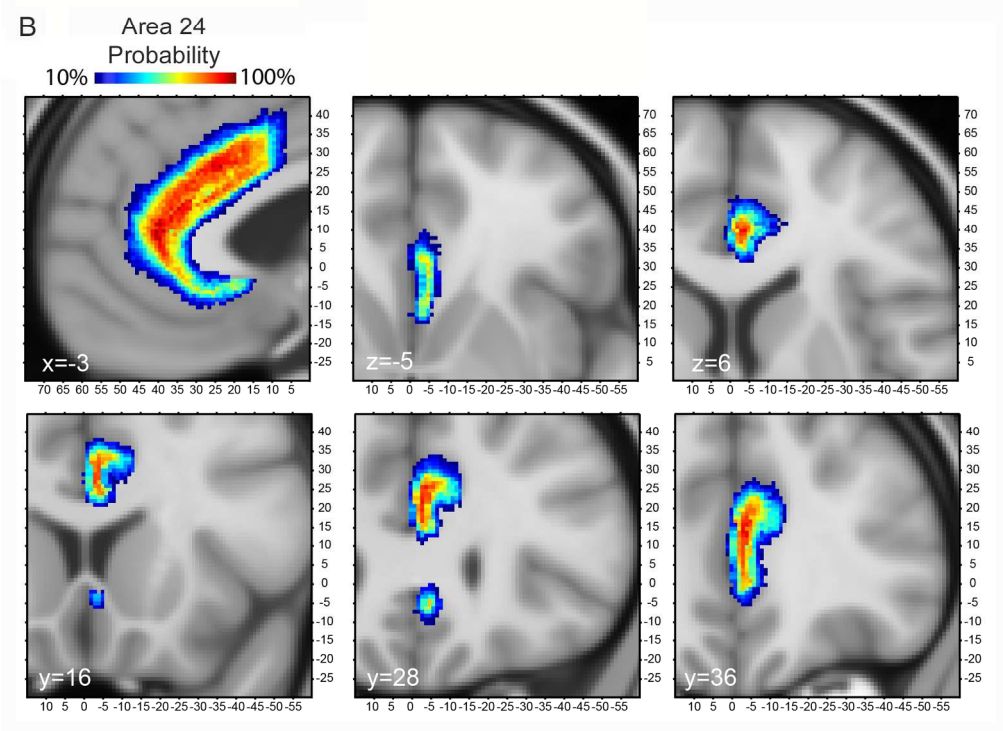

Figure 9 B Continuation

176x142mm (299 x 299 DPI)

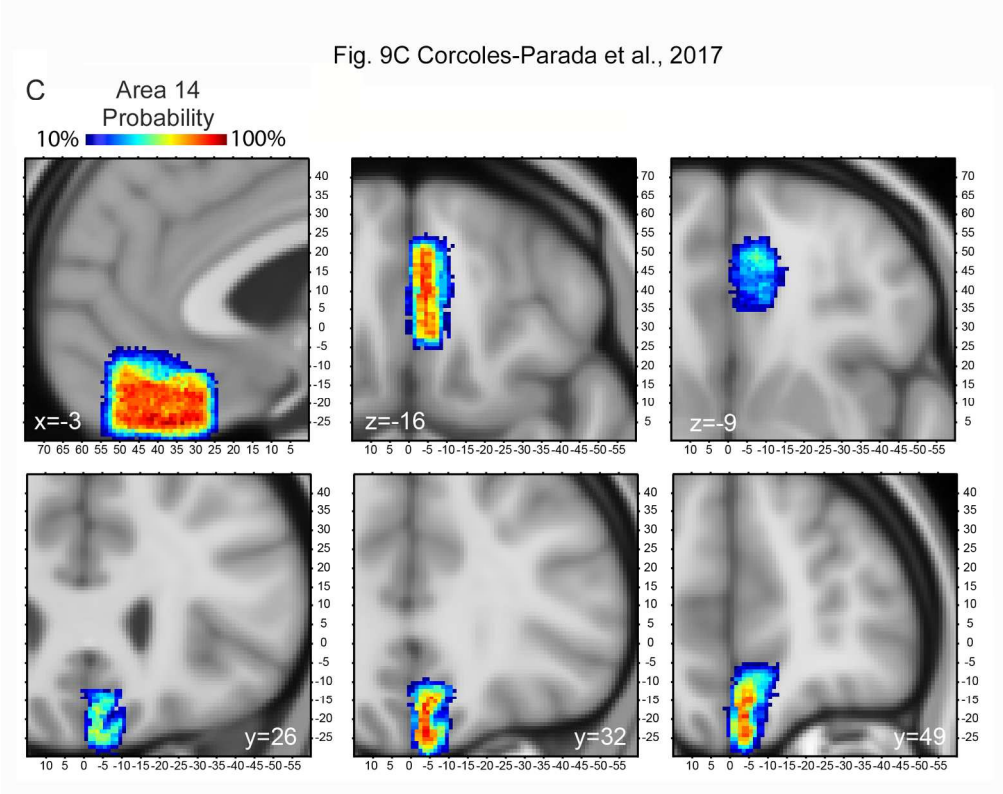

Figure 9 C Continuation

176x140mm (299 x 299 DPI)

Fig. 9D Corcoles-Parada et al., 2017

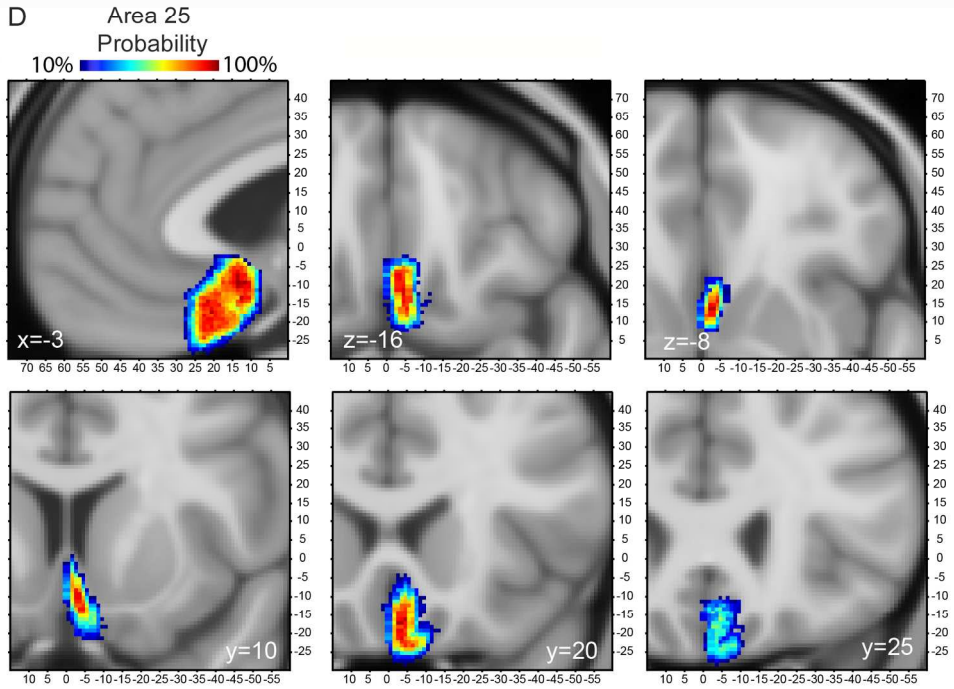

Figure 9 D Continuation

179x142mm (299 x 299 DPI)

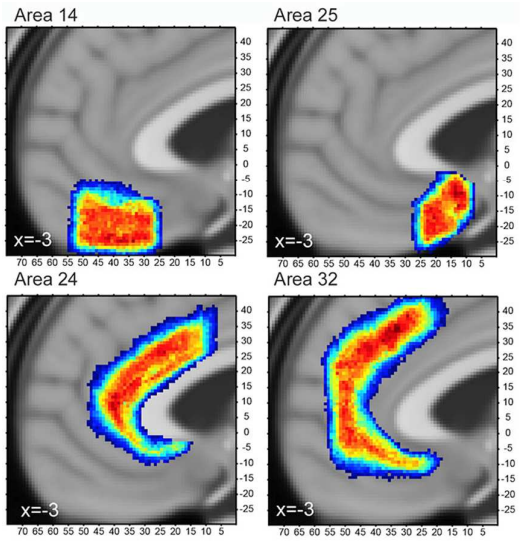

Graphical abstract

Continuous probability map of areas 14, 25, 24 and 32 for the right hemisphere in 51 MRI scans projected into the MNI average brain template.

Graphical abstract